Engineering with Computers (2022) 38 (Suppl 1):S55–S70
https://doi.org/10.1007/s00366-020-01106-8

ORIGINAL ARTICLE

# Combined analytical and numerical approach for auxetic FG-CNTRC plate subjected to a sudden load

**Xu-hao Huang**[1,2] · **Jian Yang**[1,2,3] · **Xing-er Wang**[1,2] · **Iftikhar Azim**[1,2]

Received: 7 May 2020 / Accepted: 6 July 2020 / Published online: 11 August 2020


**Abstract**
In the current work, the dynamic behavior of functionally graded carbon nanotube-reinforced composite (FG-CNTRC) plate with negative Poisson's ratio (NPR) is investigated by combining higher-order shear deformation theory and large deflection theory. First, explicit solutions are proposed to predict the effective Poisson's ratio (EPR) of the laminates. Taking carbon nanotube-reinforced composite (CNTRC) as an example, the maximum NPR is obtained for $(\pm\theta)_{3T}$ laminate as well. Results show that the EPR ($\nu_{13}^{e}$,$\nu_{23}^{e}$) can range from a positive value of 0.311 to a negative value of 0.63. For the dynamic response problem, the asymptotic solutions with a two-step perturbation approach are derived for FG-CNTRC plates to capture the relationship between the center deflection and time. Several key factors such as functionally graded distribution, variations in the elastic foundation, and thermal stress produced by changing the temperature field are considered in the subsequent analysis. Numerical simulations are carried out to examine the corresponding dynamic behavior of FG-CNTRC plates when these factors are taken into account.

**Keywords** Nonlinear dynamics · Auxetic laminated plate · Negative Poisson's ratio · Functionally graded carbon nanotubes · A two-step perturbation method

## 1 Introduction

Laminated structures made from fiber reinforced composite (FRC) are becoming of importance in many engineering fields due to excellent performance of these reinforced materials. The structural use of FRCs requires the response analysis of structures under static load and dynamic actions. A series of work has been dedicated to the study of composite plates, in particular, the investigation into their dynamic behavior [1–5]. Materials having negative Poisson's ratio (NPR) have great potential applications on the basis of their unusual properties. Related survey for the dynamic behavior of laminated plate made of auxetic honeycomb core has been performed by Li et al. [6] and Nguyen et al. [7].

In addition to the development of sandwich structures with auxetic honeycomb core, many investigations have been conducted regarding FRC laminates with NPR. Zhang et al. [8] showed that both the particular stacking sequence and the individual ply material (strongly anisotropic) were essential for the laminate to exhibit a negative Poisson's ratio. The authors also presented an optimal angle for ply and particular stacking sequence. Evans et al. [9] specially designed a software to predict the effective engineering constants. It was reported that the NPR property can be obtained by designing stacking sequences in the laminated plates. Lempriere [10] measured that the effective Poisson's ratio (EPR) in orthotropic materials was $-0.4$, occurring at $\theta = 45^{\circ}$ orientation. Clarke et al. [11] reported that the EPR of the laminates showed negative values for lay angle in a range between 15° and 30° for a $(\pm\theta)$. Herakovich [12] investigated the auxetic characteristics of laminated structure made of graphite–epoxy to determine the value of $\nu_{13}^{e}$. Such laminates exhibited a very wide range of NPR from a peak of 0.49 for a laminate with ply angle of 90° to a trough value of

✉ Jian Yang
j.yang.1@sjtu.edu.cn

1 State Key Laboratory of Ocean Engineering, School of Naval Architecture, Ocean and Civil Engineering, Shanghai Jiao Tong University, Shanghai 200240, People's Republic of China

2 Collaborative Innovation Center for Advanced Ship and Deep-Sea Exploration (CISSE), Shanghai 200240, People's Republic of China

3 School of Civil Engineering, University of Birmingham, Birmingham B15 2TT, UK

$-0.21$ for laminate with ply angle of $(\pm 25)_S$. Hine et al. [13] reported that the out-of-plane Poisson's ratio reached $-1/2$ when a high modulus of elasticity carbon fiber was used in the laminates. Matsuda et al. [14] observed that the peak values of NPR in carbon fiber-reinforced plastic laminates were around $-0.7$ when the axis was oriented at 25°. The influence of Young's modulus ratio ($E_1/E_2$), the type of resin and the volume of fraction on the ERP ($v_{13}^{e}$) of an angle-ply $[\pm\theta]_{2s}$ plate were investigated by Harkati et al. [15, 16]. It was shown that the NPR of Kevlar and carbon-reinforced composite plate was $-0.746$ at $\theta = 20°$. From the above discussion, it can be concluded that the maximum value of NPR of the laminates greatly depends on the ply orientations and stacking sequences in laminates [17].

Carbon nanotubes (CNTs) have been extensively used in the different fields of industry and research with the development of fabrication technology. CNTs are commonly deemed to be one of the most effective reinforced materials in manufacturing high strength composite material. In particular, it has led to a rapid development of carbon nanotube-reinforced composite (CNTRC) materials in the structural applications. Hence, numerous studies have been conducted on the effect of CNTs on the reinforcement of the laminates [18–20]. Moreover, the reinforced composites with functionally graded (FG) material properties have gained much attention. The concept of FG materials has been applied to multi-scale structures to present their excellent performance. Extensive studies on the forced vibration [21–23] and low impact [24–26] of FG structures have been carried out. However, all these interesting studies are limited to the structure with macroscale. Many researches have investigated the static and dynamic behavior of FG nanostructures [27–29].

Based on the above-mentioned studies, this study attempts to observe the relationships between the CNTs' laying angle and volume fractions in FG materials and EPRs. A composite laminated structure made from CNTRCs with strong anisotropy can easily develop auxetic performance. FG materials have a wide use in engineering applications and laminates with various CNT volume fractions are used to achieve their excellent mechanical properties [30]. Shen was the first investigator to analyze particular characteristics and behavior of the FG-CNTRC structures in different scales [31]. The dynamic behavior of FG-CNTRC plate resting on elastic foundations was further investigated in [32]. Considering the matrix cracks, the dynamic behavior of the hybrid laminated plate made from either FRC or CNTRC was investigated by Fan and Wang [33]. In addition to the above-mentioned studies, more studies have been carried out based on different approaches [34–38].

To the best of the authors' knowledge, the dynamic response of FG-CNTRC with NPR at different external conditions has not been reported in literature. Therefore, the primary objective of the current work is to apply the auxetic concept in FG-CNTRC laminate and study the dynamic response of these auxetic structures. Contents of this investigation are summarized as follows. The analytical model for EPR of the FG-CNTRC laminated plate is presented in Sect. 2. This model can be applied to both symmetrical and arbitrary laminates. The formulae for predicting the EPR are derived with the maximum NPR given. Further, in Sect. 3, the motion equations for the dynamic response of the plate with NPR are proposed and solved by a two-step perturbation method. The second-order ordinary differential equation (SOODE) can be obtained by applying the Galerkin method to the asymptotic solution of the motion equations. Given the initial value, the fourth-order Runge–Kutta method is used to solve the SOODE of a plate considering time variation. Several numerical cases are subsequently given in Sect. 4 regarding the dynamic behavior of FG-CNTRC plates with NPR.

## 2 Theoretical modeling of laminate with NPR

### 2.1 Theoretical approaches to evaluate effective Poisson's ratio

The effective engineering constants such as EPR are presented for the convenience of engineers in describing the mechanical behavior of the laminates. Sun and Li [17] presented the relationships for EPR for general thick laminates. However, only the extensional response was taken into consideration, while the bending and bending–extension coupling characteristics of the laminates were neglected. Therefore, their model fails to provide accurate solutions for the EPR of an asymmetric angle-ply laminated plate. Considering the effects of bending and bending–extension coupling, the general solutions of the effective Poisson's ratios for an arbitrary angle-ply laminates are derived as follows:

$$v_{13}^{e} = -\begin{vmatrix} \mathbf{A}_{13} & \mathbf{B}_{6-1} \\ \mathbf{B}_{5-3} & \mathbf{D} \end{vmatrix} \Big/ \begin{vmatrix} \mathbf{A}_{5-1} & \mathbf{B}_{6-1} \\ \mathbf{B}_{5-1} & \mathbf{D} \end{vmatrix}, \quad v_{23}^{e} = \begin{vmatrix} \mathbf{A}_{23} & \mathbf{B}_{6-2} \\ \mathbf{B}_{5-3} & \mathbf{D} \end{vmatrix} \Big/ \begin{vmatrix} \mathbf{A}_{5-2} & \mathbf{B}_{6-2} \\ \mathbf{B}_{5-2} & \mathbf{D} \end{vmatrix}, \tag{1}$$

where

$$\mathbf{A_{13}} = \begin{vmatrix} A_{21} & A_{22} & 0 & 0 & A_{26} \\ A_{31} & A_{32} & 0 & 0 & A_{36} \\ 0 & 0 & A_{44} & A_{45} & 0 \\ 0 & 0 & A_{45} & A_{55} & 0 \\ A_{61} & A_{62} & 0 & 0 & A_{66} \end{vmatrix}, \mathbf{A_{23}} = \begin{vmatrix} A_{11} & A_{12} & 0 & 0 & A_{16} \\ A_{31} & A_{32} & 0 & 0 & A_{36} \\ 0 & 0 & A_{44} & A_{45} & 0 \\ 0 & 0 & A_{45} & A_{55} & 0 \\ A_{61} & A_{62} & 0 & 0 & A_{66} \end{vmatrix},$$

$$\mathbf{A_{5-1}} = \begin{vmatrix} A_{22} & A_{23} & 0 & 0 & A_{26} \\ A_{32} & A_{33} & 0 & 0 & A_{36} \\ 0 & 0 & A_{44} & A_{45} & 0 \\ 0 & 0 & A_{45} & A_{55} & 0 \\ A_{62} & A_{63} & 0 & 0 & A_{66} \end{vmatrix}, \mathbf{A_{5-2}} = \begin{vmatrix} A_{11} & A_{13} & 0 & 0 & A_{16} \\ A_{31} & A_{33} & 0 & 0 & A_{36} \\ 0 & 0 & A_{44} & A_{45} & 0 \\ 0 & 0 & A_{45} & A_{55} & 0 \\ A_{61} & A_{63} & 0 & 0 & A_{66} \end{vmatrix},$$

$$\mathbf{B_{5-1}} = \begin{vmatrix} B_{12} & B_{13} & 0 & 0 & B_{16} \\ B_{22} & B_{23} & 0 & 0 & B_{26} \\ B_{32} & B_{33} & 0 & 0 & B_{36} \\ 0 & 0 & B_{44} & B_{45} & 0 \\ 0 & 0 & B_{45} & B_{55} & 0 \\ B_{62} & B_{63} & 0 & 0 & B_{66} \end{vmatrix}, \mathbf{B_{5-2}} = \begin{vmatrix} B_{11} & B_{13} & 0 & 0 & B_{16} \\ B_{21} & B_{23} & 0 & 0 & B_{26} \\ B_{31} & B_{33} & 0 & 0 & B_{36} \\ 0 & 0 & B_{44} & B_{45} & 0 \\ 0 & 0 & B_{45} & B_{55} & 0 \\ B_{61} & B_{63} & 0 & 0 & B_{66} \end{vmatrix}, \mathbf{B_{5-3}} = \begin{vmatrix} B_{11} & B_{12} & 0 & 0 & B_{16} \\ B_{21} & B_{22} & 0 & 0 & B_{26} \\ B_{31} & B_{32} & 0 & 0 & B_{36} \\ 0 & 0 & B_{44} & B_{45} & 0 \\ 0 & 0 & B_{45} & B_{55} & 0 \\ B_{61} & B_{62} & 0 & 0 & B_{66} \end{vmatrix}, \quad (2)$$

$$\mathbf{B_{6-1}} = \begin{vmatrix} B_{21} & B_{22} & B_{23} & 0 & 0 & B_{26} \\ B_{31} & B_{32} & B_{33} & 0 & 0 & B_{36} \\ 0 & 0 & 0 & B_{44} & B_{45} & 0 \\ 0 & 0 & 0 & B_{45} & B_{55} & 0 \\ B_{61} & B_{62} & B_{63} & 0 & 0 & B_{66} \end{vmatrix}, \mathbf{B_{6-2}} = \begin{vmatrix} B_{11} & B_{12} & B_{13} & 0 & 0 & B_{16} \\ B_{31} & B_{32} & B_{33} & 0 & 0 & B_{36} \\ 0 & 0 & 0 & B_{44} & B_{45} & 0 \\ 0 & 0 & 0 & B_{45} & B_{55} & 0 \\ B_{61} & B_{62} & B_{63} & 0 & 0 & B_{66} \end{vmatrix},$$

$$\mathbf{D} = \begin{vmatrix} D_{11} & D_{12} & D_{13} & 0 & 0 & D_{16} \\ D_{21} & D_{22} & D_{23} & 0 & 0 & D_{26} \\ D_{31} & D_{32} & D_{33} & 0 & 0 & D_{36} \\ 0 & 0 & 0 & D_{44} & D_{45} & 0 \\ 0 & 0 & 0 & D_{45} & D_{55} & 0 \\ D_{61} & D_{62} & D_{63} & 0 & 0 & D_{66} \end{vmatrix}.$$

Note that $A_{16}$, $A_{26}$, $B_{11}$, $B_{12}$, $B_{13}$, $B_{22}$, $B_{23}$, $B_{33}$, $D_{16}$, and $D_{26}$ are zero for angle-ply $\left(\pm\theta_1/\pm\theta_2/\pm\theta_1\right)$ CNTRC laminate with a symmetrical distribution of CNT. The preceding expression simplifies as follows:

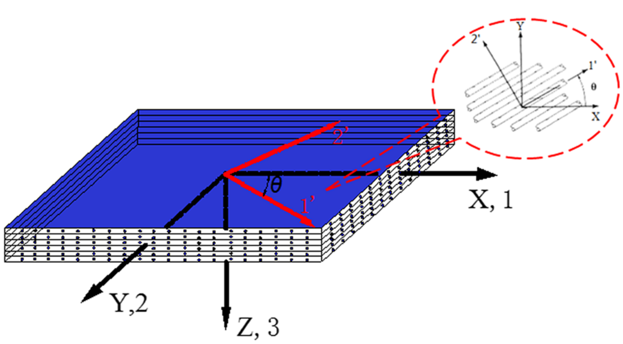


**Fig. 1** Reference coordinate system $(X, Y, Z) = (1, 2, 3)$ of the laminate and the material coordinate system consisting of longitudinal (fiber, 1′-), transverse axes (2′-), and CNT fiber orientation angle ($\theta$)

$$\nu_{ij}^{e} = \begin{cases} \dfrac{(A_{22}B_{16}-A_{12}B_{26})B_{36}+A_{13}(B_{26}^2-A_{22}D_{66})+A_{23}(A_{12}D_{66}-B_{16}B_{26})}{A_{22}B_{36}^2-2A_{23}B_{26}B_{36}+A_{23}^2D_{66}+A_{33}(B_{26}^2-A_{22}D_{66})} & (ij=13) \\ \dfrac{(A_{11}B_{26}-A_{12}B_{16})B_{36}+A_{23}(B_{26}^2-A_{11}D_{66})+A_{13}(A_{12}D_{66}-B_{16}B_{26})}{A_{11}B_{36}^2-2A_{13}B_{16}B_{36}+A_{13}^2D_{66}+A_{33}(B_{26}^2-A_{11}D_{66})} & (ij=23). \end{cases} \quad (3a)$$

In particular, for symmetrical laminates, where the material parameters of the layer are distributed symmetrically along section, the bending–extension coupling stiffnesses $B_{\mathrm{ij}}$ $(i, j = 1,2\ldots6)$ are zero. Therefore, the preceding expression simplifies as follows:

$$\nu_{ij}^{e} = \begin{cases} \dfrac{A_{16}(A_{22}A_{36}-A_{23}A_{26})+A_{13}(A_{26}^2-A_{22}A_{66})+A_{12}(A_{23}A_{66}-A_{26}A_{36})}{A_{26}^2A_{33}-2A_{23}A_{26}A_{36}+A_{23}^2A_{66}+A_{22}(A_{36}^2-A_{33}A_{66})} & (ij=13) \\ \dfrac{A_{16}^2A_{23}-A_{16}(A_{12}A_{36}+A_{13}A_{26})+A_{12}A_{13}A_{66}-A_{11}(A_{23}A_{66}-A_{26}A_{36})}{A_{16}^2A_{33}-2A_{13}A_{16}A_{36}+A_{13}^2A_{66}+A_{11}(A_{36}^2-A_{33}A_{66})} & (ij=23) \end{cases}, \quad (3b)$$

where $A_{ij}$, $B_{ij}$, $D_{ij}$ $(i, j = 1–6)$ are the plate stiffnesses, which are defined in terms of the transformed elastic coefficients $\left(\overline{C}_{ij}\right)_k$ as:

$$(A_{ij}, B_{ij}, D_{ij}) = \sum_{k=1}^{N} \int_{h_{k-1}}^{h_k} (\overline{C}_{ij})_k (1, Z, Z^2) \mathrm{d}Z \ (i,j = 1-6), \quad (4)$$

**Table 1** Mechanical parameters with different temperatures for CNTRC ply

| $V_{CN}$ | $E_{11}$ (MPa) | $E_{22}$ (MPa) | $G_{12}$ (MPa) | $v_{12}$ | $\alpha_{11}$ ($\times 10^{-6}$/K) | $\alpha_{22}$ ($\times 10^{-5}$/K) |
|---|---|---|---|---|---|---|
| $T$ = 300 K | | | | | | |
| 0.11 | 94,416.77 | 2203.74 | 822.280 | 0.3219 | 3.5830 | 5.3182 |
| 0.14 | 120,384.60 | 2297.68 | 857.328 | 0.3169 | 3.5531 | 5.1582 |
| 0.17 | 144,771.38 | 3493.88 | 1303.660 | 0.3120 | 3.5337 | 4.9979 |
| $T$ = 400 K | | | | | | |
| 0.11 | 92,708.58 | 1710.53 | 638.253 | 0.3219 | 4.2514 | 5.5640 |
| 0.14 | 118,327.70 | 1783.46 | 665.460 | 0.3169 | 4.2269 | 5.3949 |
| 0.17 | 142,387.80 | 2711.95 | 1011.91 | 0.3120 | 4.2111 | 5.2255 |
| $T$ = 500 K | | | | | | |
| 0.11 | 91,682.21 | 1217.32 | 454.222 | 0.3219 | 4.6123 | 5.8198 |
| 0.14 | 117,144.40 | 1269.22 | 473.586 | 0.3169 | 4.5940 | 5.6414 |
| 0.17 | 141,057.96 | 1930.01 | 720.144 | 0.3120 | 4.5821 | 5.4627 |

$$[\bar{C}_{ij}]^{-1} = [\bar{S}_{ij}], \tag{5}$$

where the compliance constants ($\overline{S}_{ij}$) of an orthotropic material whose principle direction 1' makes an angle $\theta$ with the $X$ axis (see Fig. 1) and $c = \cos\theta$, $s = \sin\theta$.

$$\begin{bmatrix} \bar{S}_{11} \\ \bar{S}_{12} \\ \bar{S}_{22} \\ \bar{S}_{16} \\ \bar{S}_{26} \\ \bar{S}_{66} \end{bmatrix} = \begin{bmatrix} c^4 & 2c^2s^2 & s^4 & c^2s^2 \\ c^2s^2 & c^4+s^4 & c^2s^2 & -c^2s^2 \\ s^4 & 2c^2s^2 & c^4 & c^2s^2 \\ 2c^3s & 2(cs^3-c^3s) & -2cs^3 & -cs(c^2-s^2) \\ 2cs^3 & 2(c^3s-cs^3) & -2c^3s & cs(c^2-s^2) \\ 4c^2s^2 & -8c^2s^2 & 4c^2s^2 & (c^2-s^2)^2 \end{bmatrix} \begin{bmatrix} S_{11} \\ S_{12} \\ S_{22} \\ S_{66} \end{bmatrix}, \tag{6a}$$

$$\begin{bmatrix} \bar{S}_{13} \\ \bar{S}_{23} \\ \bar{S}_{33} \end{bmatrix} = \begin{bmatrix} c^2 & s^2 & 0 \\ s^2 & c^2 & 0 \\ 0 & 0 & 1 \end{bmatrix} \begin{bmatrix} S_{13} \\ S_{23} \\ S_{33} \end{bmatrix}, \tag{6b}$$

where $S_{ij}$ are given as follows:

$$\begin{bmatrix} S_{11} & S_{12} & S_{13} \\ S_{22} & S_{23} & S_{33} \\ S_{44} & S_{55} & S_{66} \end{bmatrix} = \begin{bmatrix} 1/E_{11} & -v_{12}/E_{11} & -v_{13}/E_{11} \\ 1/E_{22} & -v_{23}/E_{22} & 1/E_{33} \\ 1/G_{23} & 1/G_{13} & 1/G_{12} \end{bmatrix}, \tag{7}$$

where the basic material parameters of each layer are introduced as follows by referring to Fig. 1.

$E_{ii}, (i = 1, 2, 3)$= Young's moduli in $i, (i = 1, 2, 3)$ directions.
$G_{ij}, (ij = 12, 13, 23)$= Shear moduli in $i - j$ planes, respectively.
$v_{ij}, (ij = 12, 13, 23)$= Poisson's ratios (the subscripts $i$ and $j$ represent the loading and strain directions, respectively).
$\alpha_{ii}, (i = 1, 2)$ = thermal expansion coefficient in the $i, (i = 1, 2)$ directions.

## 2.2 Design of CNTRC laminate with NPR

The theoretical solution presented above is capable of predicting the out-of-plane EPR of an arbitrary angle-ply laminates. A systematic investigation of the antisymmetric laminates has been carried out. Several types of CNT laminates are taken into consideration and the type of CNT volume fraction ($V_{CN}$) is given. The temperature-related material properties of CNTRCs are predicted by the extended micromechanical model [31] as summarized in Table 1. In addition, the laminated plates are also characterized by the following parameters:

**Table 2** Distribution and volume fractions of CNT for CNTRC plate

| Each ply | Types | | | | | | |
|---|---|---|---|---|---|---|---|
| | UD | FG-X | FG-O | FG-Λ | FG-V | Antisymmetric laminates in the case study | |
| | | | | | | Case A:($\pm$22)$_{3T}$ | Case A: ($\pm$70)$_{3T}$ |
| Ply1 | 0.14 | 0.17 | 0.11 | 0.11 | 0.17 | 22 | 70 |
| Ply2 | 0.14 | 0.14 | 0.14 | 0.11 | 0.17 | − 22 | − 70 |
| Ply3 | 0.14 | 0.11 | 0.17 | 0.14 | 0.14 | 22 | 70 |
| Ply4 | 0.14 | 0.11 | 0.17 | 0.14 | 0.14 | -22 | − 70 |
| Ply5 | 0.14 | 0.14 | 0.14 | 0.17 | 0.11 | 22 | 70 |
| Ply6 | 0.14 | 0.17 | 0.11 | 0.17 | 0.11 | -22 | − 70 |

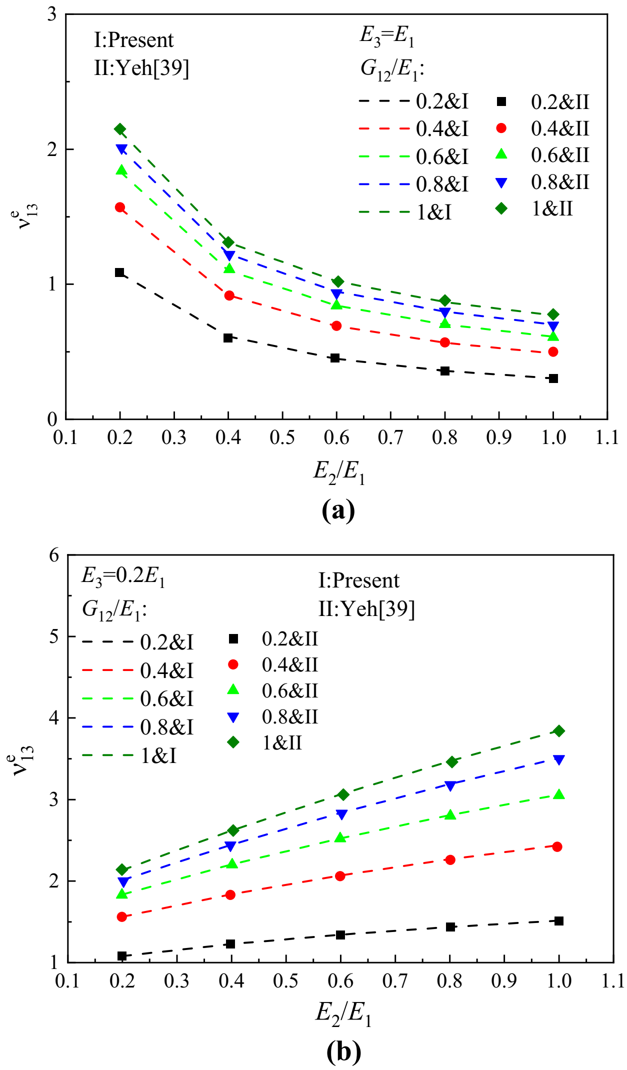


**Fig. 2** ERP ($v^e_{13}$) for laminates $(45/-45)_{4S}$ versus $E_2/E_1$ and $G_{12}/E_1$

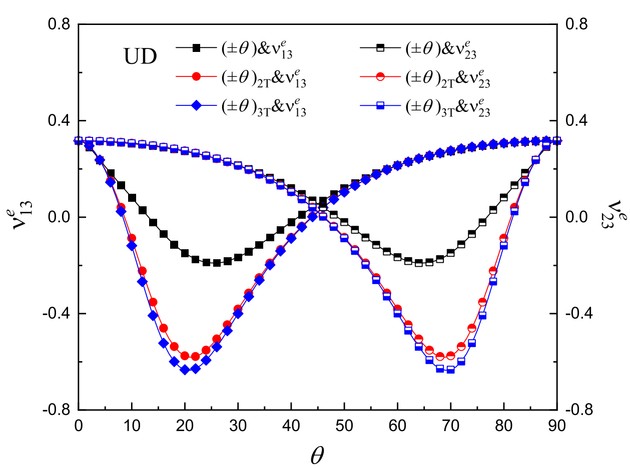


**Fig. 3** Effective Poisson's ratio ($v^e_{13}$,$v^e_{23}$) for $(\pm\theta)_{nT}$,($n$=1,2,3) laminates

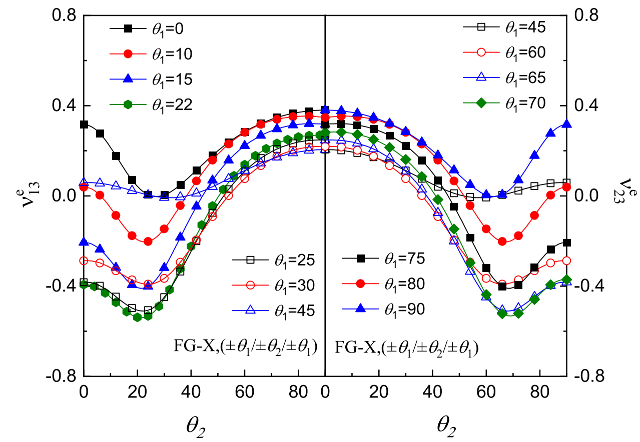


**Fig. 4** Variation of EPR with $\theta_2$ for antisymmetric angle-ply $(\pm\theta_1/\pm\theta_2/\pm\theta_1)$ plates

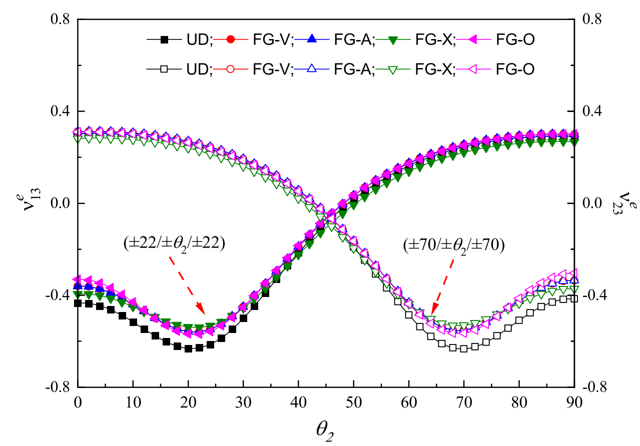


**Fig. 5** Variation of EPR with $\theta_2$ for antisymmetric angle-ply $(\pm 22/\pm\theta_2/\pm 22)$ and $(\pm 70/\pm\theta_2/\pm 70)$ plates

$$\text{Carbon nanotube volume ratio}: V_{CN} = \frac{\text{volume of carbon nanotubes}}{\text{volume of composite}},$$

$$\text{Matrix volume ratio}: V_m = \frac{\text{volume of matrix}}{\text{volume of composite}} = 1 - V_{CN},$$

where the subscripts CN and m refer to carbon nanotube and matrix, respectively. To assess how the distribution and volume fractions of CNT influence the dynamic behavior of CNTRC laminated plate, we considered five configurations as shown in Table 2. These configurations are for an identical material and one layer of the constant thickness of 0.5 mm with density $\rho = V_{CN}\rho^{CN} + V_m\rho^m$. It differs in the following characteristics: FG-Λ: $(0.11)_2/(0.14)_2/(0.17)_2$, FG-V: $(0.17)_2/(0.14)_2/(0.11)_2$, FG-X: $[0.11/0.14/0.17]_S$, FG-O: $[0.17/0.14/0.11]_S$, and uniform distribution (UD) which is used for reference.

**Table 3** NPRs ($\nu_{13}^{e}$ and $\nu_{23}^{e}$) of FG-CNTRC plates for various temperature conditions

| FG- | $(\pm 22)_{3T}$ and $\nu_{13}^{e}$ | | | $(\pm 70)_{3T}$ and $\nu_{23}^{e}$ | | |
|---|---|---|---|---|---|---|
| | 300 K | 400 K | 500 K | 300 K | 400 K | 500 K |
| UD | −0.63 | −0.74 | −0.90 | −0.63 | −0.77 | −0.97 |
| FG-V | −0.56 | −0.67 | −0.83 | −0.55 | −0.69 | −0.88 |
| FG-$\Lambda$ | −0.56 | −0.67 | −0.83 | −0.55 | −0.69 | −0.88 |
| FG-X | −0.54 | −0.65 | −0.81 | −0.53 | −0.66 | −0.86 |
| FG-O | −0.57 | −0.68 | −0.84 | −0.56 | −0.70 | −0.90 |

As a part of the verification of the proposed method, Fig. 2 shows the comparisons of the EPR ($\nu_{13}^{e}$) of Yeh [39] with the present solutions of symmetrical laminates. The material properties of the laminates are taken as: $E_1 = 200$GPa, $\nu_{12} = 0.2$, $\nu_{31} = 0.4$, $\nu_{32} = 0.6$. The effective Poisson's ratios $\nu_{13}^{e}$ are calculated for a range of relative elastic modulus $E_2/E_1$. As described in Fig. 2, the values of $\nu_{13}^{e}$ of laminates $(45/-45)_{4S}$ with $E_3 = E_1$ and $E_3 = 0.2E_1$ are plotted with varying relative elastic modulus $G_{12}/E_1$. The proposed predictions of $\nu_{13}^{e}$ agree well with the results of Yeh [39].

The CNT distribution patterns significantly affect the mechanical behavior of composites with identical $V_{CN}$. The effects of CNTs orientation angle on the buckling behavior of CNTRC plate were investigated by Zhang et al. [40] and Jam and Maghamikia [41]. The above researches made the assumption that CNT fibers with sufficient length have to be placed in a specified direction. This assumption is also adopted in this study.

In this study, the auxetic concept of FRC laminates is extended to design FG-CNTRC laminate with NPR. The mechanism of auxetic laminates was reported theoretically by Yeh et al. [42, 43]. In their study, the detailed theory for a $(\theta_1/\theta_2)_S$ laminate can be found. The explicit solutions in Eq. (1) are used to study the effect of the stacking sequence and the FG type on the EPR ($\nu_{13}^{e}$,$\nu_{23}^{e}$). Figure 3 plots the effects of the CNT orientation angle ($\theta$) on the EPR of the $[\pm\theta]_{nT}$, ($n = 1,2,3$) UD plates. The variety of $\nu_{13}^{e}$ and $\nu_{23}^{e}$ versus $\theta$ is same for all the antisymmetric plates. It is found that the value of $\nu_{13}^{e}$ decreases by increasing the magnitude of $\theta$. It attains a minimum negative value between 20° and 25° after which it reaches its maximum value. $\nu_{23}^{e}$ is positive at $\theta$=90° and decreases rapidly after attaining its maximum negative value between 65° and 70°. For the three types of antisymmetric laminates with same thickness, the minimum negative value of EPR occurs at CNT orientation $(\pm\theta)_{3T}$. Moreover, the EPRs for FG-X plate is plotted in Fig. 4. The curves describe the variation in EPR for FG-X, $(\pm\theta_1/\pm\theta_2/\pm\theta_1)$, $0 \le \theta_2 \le 90$ with equal thickness layers. These curves show the effect of both $\theta_2$ and $\theta_1$. In Fig. 5, the values of NPR for two antisymmetric FG-CNTRCs consisting of six layers, $(\pm 22/\pm\theta_2/\pm 22)$ and $(\pm 70/\pm\theta_2/\pm 70)$, are plotted with varying orientation angle $\theta_2$. The out-of-plane Poisson's ratio has its most negative value at $(\pm\theta)_{3T} = (\pm 22)_{3T}$ for $\nu_{13}^{e}$ and $(\pm\theta)_{3T} = (\pm 70)_{3T}$ for $\nu_{23}^{e}$. They correspond to a reflection of the value of EPR at about 45° orientations. In all the FG-CNTRC plates, $(\pm\theta)_{3T} = (\pm 22)_{3T} = (\pm 70)_{3T}$ is considered. Table 3 shows the values of the minimum NPR for these two CNTRC plates at temperature ranging from 300 K to 500 K.

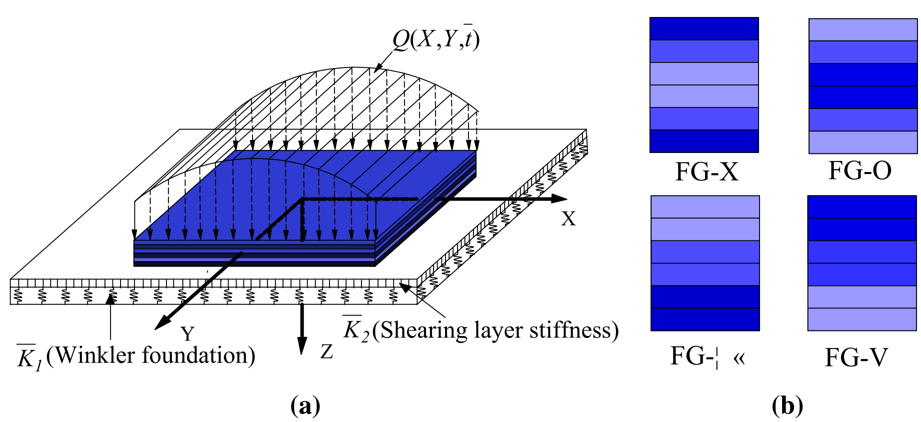


**Fig. 6** Various types of FG-CNTRC plates and the reference system adopted

## 3 Theoretical modeling of nonlinear dynamic response

### 3.1 Motion equations for nonlinear dynamic response

Laminates consist of layers of composites reinforced with CNTRC. Consider a square laminated plate composed of six plies of equal thickness ($t_k$= 0.5 mm) with each side $a = b$=60 mm resting on a continuous elastic foundation as shown in Fig. 6. Figure 6a defines the coordinate system to be used in developing the FG-CNTRC plate analysis. The $XYZ$ coordinate system is assumed to have its origin on the middle face of the plate, so that the middle surface lies on the $XY$-plane. The displacement at a point on the $X$, $Y$, and $Z$ directions is $\bar{U}$,$\bar{V}$, and $\bar{W}$, respectively.

The simply supported plate is resting on a two-parameter elastic foundation including the Winkler foundation ($\bar{K}_1$) and shearing layer stiffness ($\bar{K}_2$). The force per unit $p_0(X, Y, \bar{t})$ is given by:

$$p_0 = \bar{K}_1\bar{W} - \bar{K}_2\left(\partial^2\bar{W}/\partial X^2 + \partial^2\bar{W}/\partial Y^2\right). \tag{8}$$

The method of analysis is based on the third-order shear deformation theory [44] for the laminated plate undergoing large deflection. The effect of the elevated temperature is considered by introducing thermal stress resultants $\bar{N}^{\mathrm{T}}$ ,$\bar{M}^{\mathrm{T}}$, and $\overline{P}^{\mathrm{T}}$ as shown in Appendix 1. In all the cases, a suddenly applied load $Q$ is considered. The motion equations are given as follows:

$$\tilde{L}_{11}(\bar{W}) - \tilde{L}_{12}(\bar{\Psi}_x) - \tilde{L}_{13}(\bar{\Psi}_y) + \tilde{L}_{14}(\bar{F}) - \tilde{L}_{15}(\bar{N}^T) - \tilde{L}_{16}(\bar{M}^T) + p_0 = \tilde{L}_{17}(\ddot{\bar{W}}) + \tilde{L}(\bar{W},\bar{F}) + I_8\left(\frac{\partial\ddot{\bar{\Psi}}_x}{\partial X} + \frac{\partial\ddot{\bar{\Psi}}_y}{\partial Y}\right) + Q, \tag{9}$$

$$\tilde{L}_{21}(\bar{F}) + \tilde{L}_{22}(\bar{\Psi}_x) + \tilde{L}_{23}(\bar{\Psi}_y) - \tilde{L}_{24}(\bar{W}) - \tilde{L}_{25}(\bar{N}^T) = -\frac{1}{2}\tilde{L}(\bar{W},\bar{W}), \tag{10}$$

$$\tilde{L}_{31}(\bar{W}) + \tilde{L}_{32}(\bar{\Psi}_x) - \tilde{L}_{33}(\bar{\Psi}_y) + \tilde{L}_{34}(\bar{F}) - \tilde{L}_{35}(\bar{N}^T) - \tilde{L}_{36}(\bar{S}^T) = I_9\frac{\partial\ddot{\bar{W}}}{\partial X} + I_{10}\ddot{\bar{\Psi}}_x, \tag{11}$$

$$\tilde{L}_{41}(\bar{W}) - \tilde{L}_{42}(\bar{\Psi}_x) + \tilde{L}_{43}(\bar{\Psi}_y) + \tilde{L}_{44}(\bar{F}) - \tilde{L}_{45}(\bar{N}^T) - \tilde{L}_{46}(\bar{S}^T) = I_9\frac{\partial\ddot{\bar{W}}}{\partial Y} + I_{10}\ddot{\bar{\Psi}}_y, \tag{12}$$

where the nonlinear operator ($\tilde{L}()$) and a stress function ($\bar{F}$) can be expressed as follows:

$$\tilde{L}(\ ) = \frac{\partial^2}{\partial X^2}\frac{\partial^2}{\partial Y^2} - 2\frac{\partial^2}{\partial X\partial Y}\frac{\partial^2}{\partial X\partial Y} + \frac{\partial^2}{\partial Y^2}\frac{\partial^2}{\partial X^2}, \tag{13}$$

$$\bar{N}_x = \partial^2\bar{F}/\partial Y^2, \bar{N}_y = \partial^2\bar{F}/\partial X^2, \bar{N}_{xy} = -\partial^2\bar{F}/\partial X\partial Y, \tag{14}$$

$\bar{\Psi}_x$ and $\bar{\Psi}_y$ denote rotation about the $Y$- and $X$-axes, respectively. The coefficients $S_{ij}$ and generalized inertias $I_i$ are given in Appendix 1. The linear operators ($\tilde{L}_{ij}()$) introduced in the above motion equations are defined from [45].

Depending upon the in-plane behavior at the edges, two boundary conditions (BCs) used are:

$$\text{At } X = 0, a: \begin{cases} \bar{W} = \bar{\Psi}_y = \bar{M}_x = \bar{P}_x = 0 \\ \int_0^b \bar{N}_x \,\mathrm{d}Y + \sigma_x bh = 0 \,(\text{movable}) \\ \bar{U} = 0 \quad (\text{immovable}), \end{cases} \tag{15a}$$

$$\text{At } Y = 0, b: \begin{cases} \bar{W} = \bar{\Psi}_x = \bar{M}_y = \bar{P}_y = 0 \\ \int_0^a \bar{N}_y \,\mathrm{d}X + \sigma_y ah = 0 \,(\text{movable}) \\ \bar{V} = 0 \quad (\text{immovable}), \end{cases} \tag{15b}$$

in which the quantities ($\bar{M}_x$, $\bar{M}_y$) denote the flexural moments and ($\bar{P}_x$,$\bar{P}_y$) represent the higher-order moments given by [45].

In Eq. (15), the immovable in-plane BCs are converted to integral form:

$$\int_0^b\int_0^a \frac{\partial\bar{U}}{\partial X}\mathrm{d}X\mathrm{d}Y = 0, \tag{16a}$$

$$\int_0^a\int_0^b \frac{\partial\bar{V}}{\partial Y}\mathrm{d}Y\mathrm{d}X = 0, \tag{16b}$$

where

$$\frac{\partial\bar{U}}{\partial X} = A_{11}^*\frac{\partial^2\bar{F}}{\partial Y^2} + A_{12}^*\frac{\partial^2\bar{F}}{\partial X^2} + \left(B_{11}^* - \frac{4E_{11}^*}{3h^2}\right)\frac{\partial\bar{\Psi}_x}{\partial X} + \left(B_{12}^* - \frac{4E_{12}^*}{3h^2}\right)\frac{\partial\bar{\Psi}_y}{\partial Y} - \frac{4}{3h^2}\left(E_{21}^*\frac{\partial^2\bar{W}}{\partial X^2} + E_{22}^*\frac{\partial^2\bar{W}}{\partial Y^2}\right) - \frac{1}{2}\left(\frac{\partial\bar{W}}{\partial X}\right)^2 - \left(A_{11}^*\bar{N}_x^T + A_{12}^*\bar{N}_y^T\right), \tag{17a}$$

$$\frac{\partial\bar{V}}{\partial Y} = A_{22}^*\frac{\partial^2\bar{F}}{\partial X^2} + A_{12}^*\frac{\partial^2\bar{F}}{\partial Y^2} + \left(B_{21}^* - \frac{4E_{21}^*}{3h^2}\right)\frac{\partial\bar{\Psi}_x}{\partial X} + \left(B_{22}^* - \frac{4E_{22}^*}{3h^2}\right)\frac{\partial\bar{\Psi}_y}{\partial Y} - \frac{4}{3h^2}\left(E_{21}^*\frac{\partial^2\bar{W}}{\partial X^2} + E_{22}^*\frac{\partial^2\bar{W}}{\partial Y^2}\right) - \frac{1}{2}\left(\frac{\partial\bar{W}}{\partial X}\right)^2 - (A_{12}^*\bar{N}_x^T + A_{22}^*\bar{N}_y^T), \tag{17b}$$

where the reduced stiffnesses ($A_{ij}^*$, $B_{ij}^*$, $D_{ij}^*$, $E_{ij}^*$, $F_{ij}^*$,$H_{ij}^*$) are the functions of the geometry, materials properties, and the stacking sequence of the individual as given in Appendix 2.

### 3.2 Solution of the nonlinear equations

The nonlinear motion equations for the dynamic response can be solved by a two-step perturbation approach proposed by Shen [45]. Equations (9)–(12) can be converted to dimensionless forms by defining the following dimensionless parameters:

$$L_{11}(W) - L_{12}(\Psi_x) - L_{13}(\Psi_y) + \gamma_{14} L_{14}(F) - L_{16}(M^T) = L_{17}(\ddot{W}) + \lambda_q - K_1 W + K_2 \nabla^2 W + \gamma_{14}\beta^2 L(W,F) + \gamma_{80}\left(\frac{\partial \ddot{\Psi}_x}{\partial x} + \beta \frac{\partial \ddot{\Psi}_y}{\partial y}\right), \tag{18}$$

$$L_{21}(F) + \gamma_{24}L_{22}(\Psi_x) + \gamma_{24}L_{23}(\Psi_y) - \gamma_{24}L_{24}(W) = -\frac{1}{2}\gamma_{24}\beta^2 L(W,W), \tag{19}$$

$$L_{31}(W) + L_{32}(\Psi_x) - L_{33}(\Psi_y) + \gamma_{14}L_{34}(F) - L_{36}(S^T) = \gamma_{90}\frac{\partial \ddot{W}}{\partial x} + \gamma_{10}\ddot{\Psi}_x, \tag{20}$$

$$L_{41}(W) - L_{42}(\Psi_x) + L_{43}(\Psi_y) + \gamma_{14}L_{44}(F) - L_{46}(S^T) = \gamma_{90}\beta\frac{\partial \ddot{W}}{\partial y} + \gamma_{10}\ddot{\Psi}_y, \tag{21}$$

where it is convenient to introduce dimensionless parameters and nonlinear operator ($L()$).

$$\begin{bmatrix} A_x^T & D_x^T & F_x^T \\ A_y^T & D_y^T & F_y^T \end{bmatrix} = -\sum_{K=1}^{N}\int_{h_{k-1}}^{h_k}\begin{bmatrix} A_x \\ A_y \end{bmatrix}_k (1, Z, Z^3)\mathrm{d}Z, \tag{23}$$

In Eqs. (18)–(21), the dimensionless linear operators ($L_{ij}()$) are defined in [45].

Substitution of dimensionless parameters into Eq. (15) yields:

$$\text{At } x=0,a: \begin{cases} W = \Psi_y = M_x = P_x = 0 \\ \delta_x = 0 (\text{immovable edges}) \\ \frac{1}{\pi}\int_0^{\pi} \beta^2 \frac{\partial^2 F}{\partial y^2}\mathrm{d}y + 4\lambda_x\beta^2 = 0\, (\text{movable edges}), \end{cases} \tag{24a}$$

$$\text{At } y=0,b: \begin{cases} W = \Psi_x = M_y = P_y = 0 \\ \delta_y = 0 (\text{immovable edges}) \\ \frac{1}{\pi}\int_0^{\pi} \frac{\partial^2 F}{\partial x^2}\mathrm{d}x + 4\lambda_y = 0\, (\text{movable edges}) \end{cases}, \tag{24b}$$

where $\delta_x$ and $\delta_y$ are given as:

$$\begin{aligned}
&(x,y,\beta) = \left(\pi\frac{X}{a}, \pi\frac{Y}{b}, \frac{a}{b}\right), (W,F) = \left(\frac{\bar{W}}{[D_{11}^* D_{22}^* A_{11}^* A_{22}^*]^{1/4}}, \frac{\bar{F}}{[D_{11}^* D_{22}^*]^{1/2}}\right),\\
&(\Psi_x, \Psi_y) = \frac{a}{\pi}\frac{(\bar{\Psi}_x, \bar{\Psi}_y)}{[D_{11}^* D_{22}^* A_{11}^* A_{22}^*]^{1/4}}, (\gamma_{14}, \gamma_{24}, \gamma_5) = \left(\left(\frac{D_{22}^*}{D_{11}^*}\right)^{1/2}, \left(\frac{A_{11}^*}{A_{22}^*}\right)^{1/2}, -\frac{A_{12}^*}{A_{22}^*}\right),\\
&(\gamma_{T1}, \gamma_{T2}) = \frac{a^2}{\pi^2}\frac{(A_x^T, A_y^T)}{[D_{11}^* D_{22}^*]^{1/2}}, (\gamma_{T3}, \gamma_{T4}, \gamma_{T6}, \gamma_{T7}) = \frac{a^2}{\pi^2 h D_{11}^*}\left(D_x^T,\ D_y^T,\ \frac{4}{3h^2}F_x^T,\ \frac{4}{3h^2}F_y^T\right),\\
&(M_x,\ P_x) = \frac{a^2}{\pi^2}\frac{1}{D_{11}^*[D_{11}^* D_{22}^* A_{11}^* A_{22}^*]^{1/4}}\left(\bar{M}_x,\ \frac{4}{3h^2}\bar{P}_x\right),\\
&(K_1, K_2) = \frac{a^2}{\pi^2 D_{11}^*}\left(a^2\bar{K}_1,\ \bar{K}_2\right), (k_1, k_2) = \frac{b^2}{E_0 h^3}\left(b^2\bar{K}_1,\ \bar{K}_2\right),\\
&t = \frac{\pi\bar{t}}{a}\sqrt{\frac{E_0}{\rho_0}}, \gamma_{170} = -\frac{I_1 E_0 a^2}{\pi^2\rho_0 D_{11}^*}, \gamma_{171} = \frac{4E_0(I_5 I_1 - I_4 I_2)}{3\rho_0 h^2 I_1 D_{11}^*},\\
&(\gamma_{80}, \gamma_{90}, \gamma_{10}) = (I_8, I_9, I_{10})\frac{E_0}{\rho_0 D_{11}^*}, (\lambda_x,\ \lambda_y) = \frac{(\sigma_x b^2,\ \sigma_y a^2)h}{4\pi^2[D_{11}^* D_{22}^*]^{1/2}},\\
&\lambda_q = \frac{Qa^4}{\pi^4 D_{11}^*[D_{11}^* D_{22}^* A_{11}^* A_{22}^*]^{1/4}}, L(\ ) = \frac{\partial^2}{\partial X^2}\frac{\partial^2}{\partial Y^2} - 2\frac{\partial^2}{\partial X\partial Y}\frac{\partial^2}{\partial X\partial Y} + \frac{\partial^2}{\partial Y^2}\frac{\partial^2}{\partial X^2},
\end{aligned} \tag{22}$$

in which $E_0 = E^m$, $\rho_0 = \rho^m$, $A_x^T$, $D_x^T$, $F_x^T$, etc. are the functions of the thickness. $A_x$, $A_y$ can be defined by:

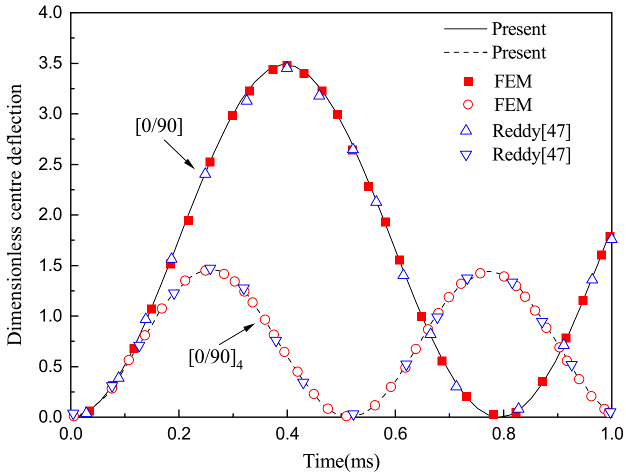


**Fig. 7** Comparison of the dynamic response curves for angle-ply $[0/90]_n$ $(n=1,4)$ laminated plates under a suddenly applied load

$$
\begin{aligned}
\tilde{W}(x,y,\tau,\varepsilon) &= \varepsilon w_1(x,y,\tau) + \varepsilon^2 w_2(x,y,\tau) + \varepsilon^3 w_3(x,y,\tau) + \cdots \\
\tilde{\Psi}_x(x,y,\tau,\varepsilon) &= \varepsilon \psi_{x1}(x,y,\tau) + \varepsilon^2 \psi_{x2}(x,y,\tau) + \varepsilon^3 \psi_{x3}(x,y,\tau) + \cdots \\
\tilde{\Psi}_y(x,y,\tau,\varepsilon) &= \varepsilon \psi_{y1}(x,y,\tau) + \varepsilon^2 \psi_{y2}(x,y,\tau) + \varepsilon^3 \psi_{y3}(x,y,\tau) + \cdots \\
\tilde{F}(x,y,\tau,\varepsilon) &= f_1(x,y,\tau) + \varepsilon f_2(x,y,\tau) + \varepsilon^2 f_3(x,y,\tau) + \cdots \\
\lambda_q(x,y,\tau,\varepsilon) &= \varepsilon \lambda_1(x,y,\tau) + \varepsilon^2 \lambda_2(x,y,\tau) + \varepsilon^3 \lambda_3(x,y,\tau) + \cdots
\end{aligned}
\tag{26}
$$

Following the perturbation solutions procedure, one assumes that the following form of the first term of $w_j$ $(x, y,\tau)$ satisfies the simply supported BCs:

$$w_1(x,y,\tau) = A_{11}^{(1)}(\tau)\sin mx \sin ny, \tag{27}$$

where the terms $(m, n)$ are used to describe the waveform. The following initial BCs are adopted in the present work

$$\widetilde{W}|_{t=0} = \frac{\partial \widetilde{W}}{\partial t}|_{t=0} = 0, \widetilde{\Psi}_x|_{t=0} = \frac{\partial \widetilde{\Psi}_x}{\partial t}|_{t=0} = 0, \widetilde{\Psi}_y|_{t=0} = \frac{\partial \widetilde{\Psi}_y}{\partial t}|_{t=0} = 0. \tag{28}$$

Motion equations converted to their perturbation expan-

$$
\begin{aligned}
\delta_x = \frac{1}{4\pi^2\beta^2\gamma_{24}} \int_0^{\pi}\int_0^{\pi} \Bigg[ & \gamma_{24}^2\beta^2\frac{\partial^2 F}{\partial y^2} - \gamma_5\frac{\partial^2 F}{\partial x^2} + \gamma_{24}\left(\gamma_{511}\frac{\partial \Psi_x}{\partial x} + \gamma_{223}\beta\frac{\partial \Psi_y}{\partial y}\right) \\
& - \gamma_{24}\left(\gamma_{244}\beta^2\frac{\partial^2 W}{\partial y^2} + \gamma_{611}\frac{\partial^2 W}{\partial x^2} + 2\gamma_{516}\beta\frac{\partial^2 W}{\partial x\partial y}\right) \\
& - \frac{1}{2}\gamma_{24}\left(\frac{\partial W}{\partial x}\right)^2 + (\gamma_{24}^2\gamma_{T1} - \gamma_5\gamma_{T2})\Delta T\Bigg]\mathrm{d}x\mathrm{d}y,
\end{aligned}
\tag{25a}
$$

$$
\begin{aligned}
\delta_y = \frac{1}{4\pi^2\beta^2\gamma_{24}} \int_0^{\pi}\int_0^{\pi} \Bigg[ & \frac{\partial^2 F}{\partial x^2} - \gamma_5\beta^2\frac{\partial^2 F}{\partial y^2} + \gamma_{24}\left(\gamma_{220}\frac{\partial \Psi_x}{\partial x} + \gamma_{522}\beta\frac{\partial \Psi_y}{\partial y}\right) \\
& - \gamma_{24}\left(\gamma_{240}\frac{\partial^2 W}{\partial x^2} + \gamma_{622}\beta^2\frac{\partial^2 W}{\partial y^2} + 2\gamma_{526}\beta\frac{\partial^2 W}{\partial x\partial y}\right) \\
& - \frac{1}{2}\gamma_{24}\beta^2\left(\frac{\partial W}{\partial y}\right)^2 + (\gamma_{T2} - \gamma_5\gamma_{T1})\Delta T\Bigg]\mathrm{d}x\mathrm{d}y,
\end{aligned}
\tag{25b}
$$

with $\gamma_{ijk}$ given in Shen [45].

The solutions for Eqs. (18)–(21) consist of an additional deflection term and initial deflection term as a result of the varying temperature. For convenience, we only discuss the solution process of the first term. The solutions of initial deflections can be obtained in the same way [46]. By considering $\tau = \varepsilon t$, the solution equations can be expanded as a function with a small perturbation parameter $\varepsilon^j (j = 1, 2, 3, \ldots)$ as given below:

sions are derived from the substitution of Eq. (26) into Eqs. (18)–(21). The asymptotic solutions obtained for the perturbation equations with order equal to $\varepsilon = 1, 2, 3$ are given below:

$$
\begin{aligned}
\tilde{W}(x,y,t) = \varepsilon\left[A_{11}^{(1)}(t)\sin mx\sin ny\right] + \varepsilon^3\Big[ & A_{13}^{(3)}(t)\sin mx\sin 3ny \\
& + A_{31}^{(3)}(t)\sin 3mx\sin ny\Big] + O(\varepsilon^4),
\end{aligned}
\tag{29}
$$

$$
\begin{aligned}
\tilde{\Psi}_x(x,y,t) = & \varepsilon\left[C_{11}^{(1)}(t) + \ddot{C}_{11}^{(3)}(t)\right]\cos mx\sin ny + \varepsilon^2 C_{20}^{(2)}(t)\sin 2mx \\
& + \varepsilon^3\left[C_{13}^{(3)}(t)\cos mx\sin 3ny + C_{31}^{(3)}(t)\cos 3mx\sin ny\right] + O(\varepsilon^4),
\end{aligned}
\tag{30}
$$

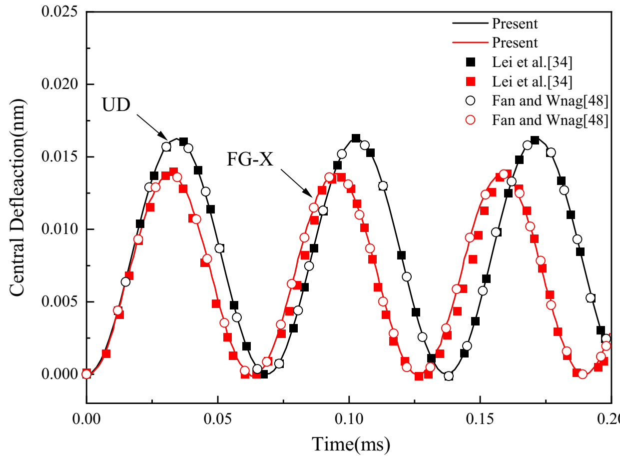


**Fig. 8** Comparison of the dynamic response curves for CNTRC laminated plate under a suddenly applied load. The distribution of CNTs of the FG-X are expressed as $2(2|Z|/h) \times V_{cn}$

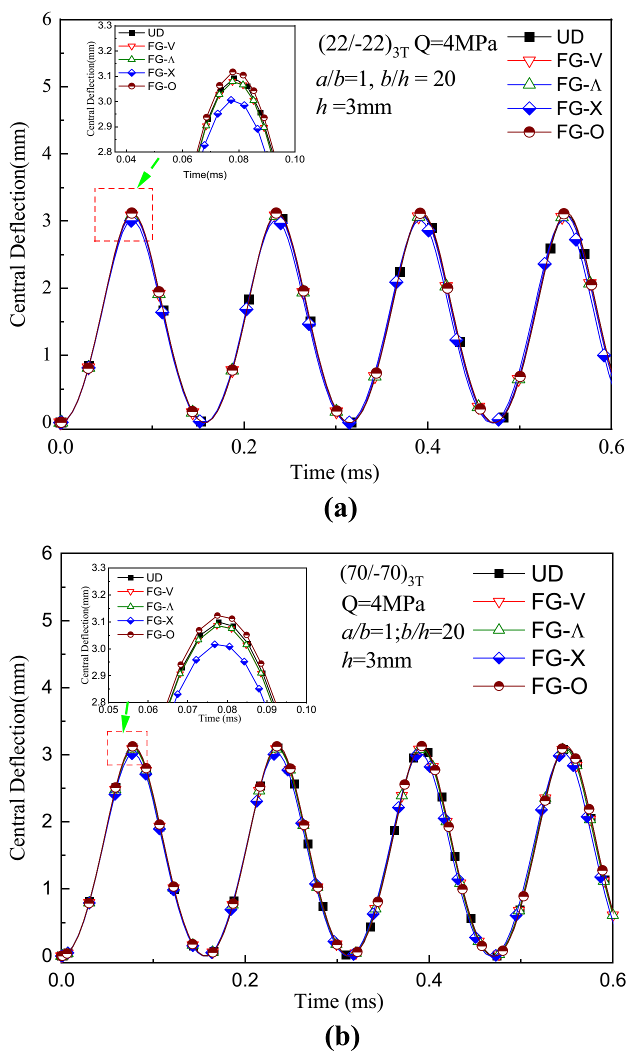


**Fig. 9** Central deflection versus time ($t$) of CNTRC plates with NPR

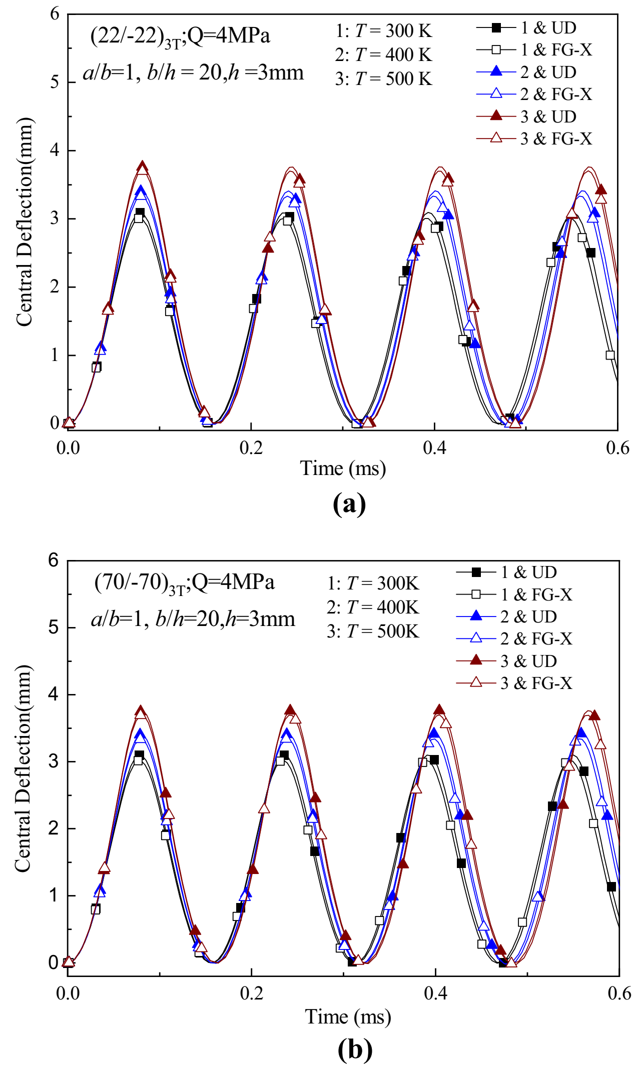


**Fig. 10** Deflection versus time ($t$) of CNTRC plates with various temperature conditions ($T = 300$ K, 400 K, 500 K)

$$\begin{aligned}\tilde{\Psi}_y(x,y,t) &= \varepsilon\left[D^{(1)}_{11}(t) + \ddot{D}^{(3)}_{11}(t)\right]\sin mx\cos ny \\ &\quad + \varepsilon^2 D^{(2)}_{02}(t)\sin 2ny + \varepsilon^3\Big[D^{(3)}_{13}(t)\sin mx\cos 3ny \\ &\quad + D^{(3)}_{31}(t)\sin 3mx\cos ny\Big] + O(\varepsilon^4),\end{aligned} \tag{31}$$

$$\begin{aligned}\tilde{F}(x,y,t) &= -B^{(0)}_{00}y^2/2 - b^{(0)}_{00}x^2/2 + \varepsilon\left[B^{(1)}_{11}(t) + \ddot{B}^{(3)}_{11}(t)\right]\cos mx\cos ny \\ &\quad + \varepsilon^2\Big(-B^{(2)}_{00}y^2/2 - b^{(2)}_{00}x^2/2 \\ &\quad + B^{(2)}_{02}(t)\cos 2ny + B^{(2)}_{20}(t)\cos 2mx\Big) \\ &\quad + \varepsilon^3\Big[B^{(3)}_{13}(t)\cos mx\cos 3ny \\ &\quad + B^{(3)}_{31}(t)\cos 3mx\cos ny\Big] + O(\varepsilon^4),\end{aligned} \tag{32}$$

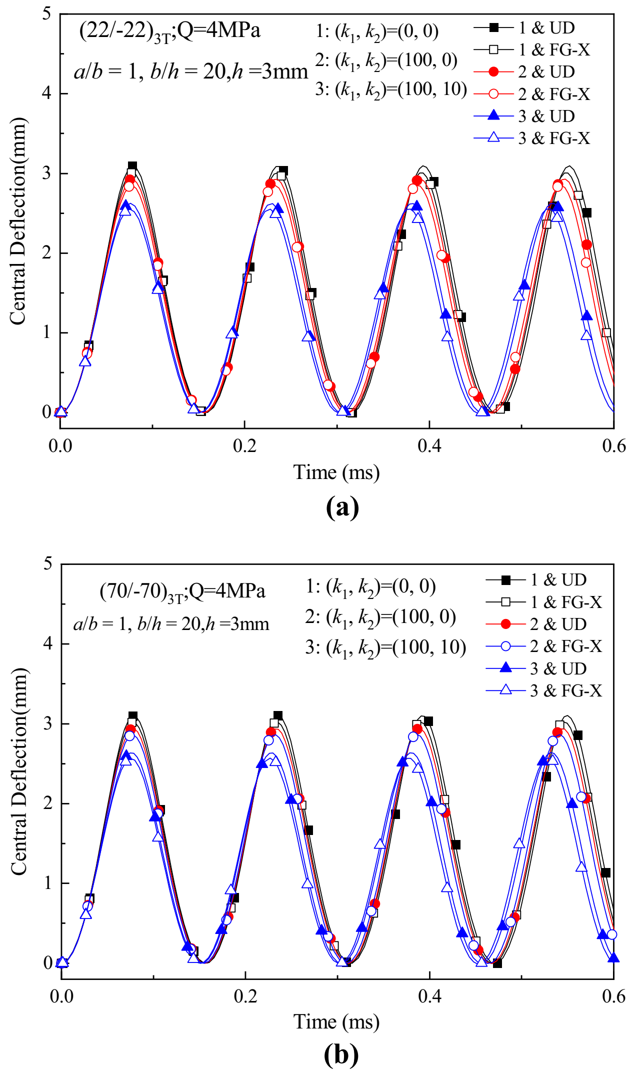


**Fig. 11** Deflection versus time ($t$) of CNTRC plates with various elastic foundation constants at the reference temperature ($T$ = 300 K)

$$\lambda_q(x,y,t) = \left[g_1 A_{11}^{(1)}(t) + g_4 \ddot{A}_{11}^{(1)}(t)\right]\varepsilon \sin mx \sin ny + \left(\varepsilon A_{11}^{(1)}(t)\right)^3 g_3 \sin mx \sin ny + O(\varepsilon^4). \quad (33)$$

In Eq. (33), $\varepsilon A_{11}^{(1)}(t)$ is considered as the second perturbation parameter which is the function of the deflection by taking $(x, y) = (\pi/2m, \pi/2n)$

$$\varepsilon A_{11}^{(1)}(t) = \widetilde{W}_m - \Theta_1 \widetilde{W}_m^3 + \cdots \quad (34)$$

Substituting Eq. (34) into Eq. (33) and applying Galerkin procedure yielded the Eq. (33) which can be re-written as:

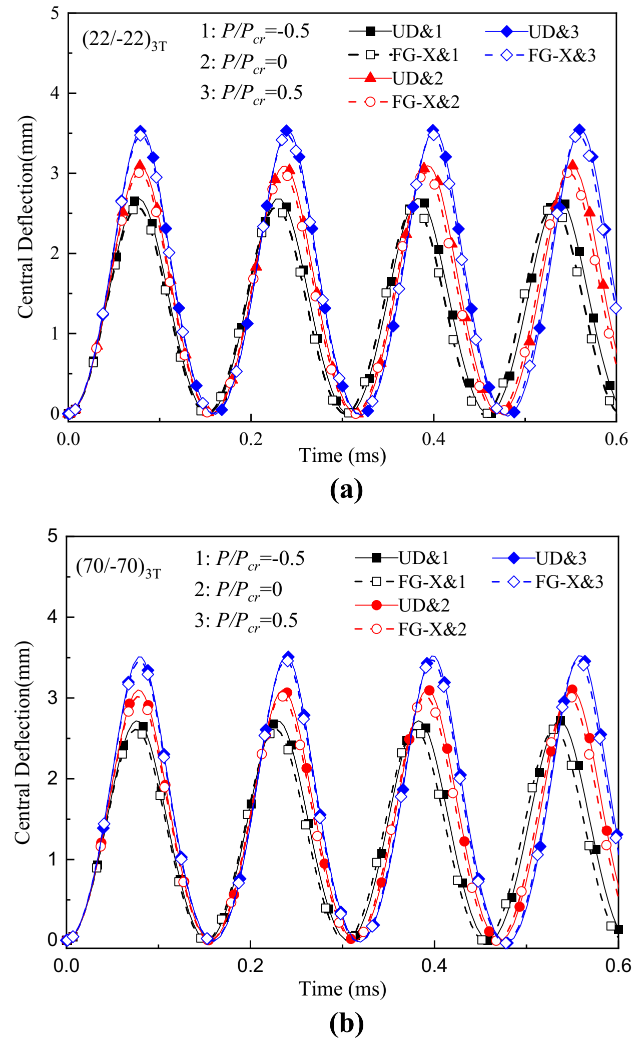


**Fig. 12** Deflection versus time ($t$) of CNTRC plates with in-plane movable edges

with $g_{4j}$ ($j$ = 0,1,2,3) defined in Eqs. (45)–(47) of the Appendix 3, and

$$\bar{\lambda}_q(t) = \frac{4}{\pi^2}\int_0^\pi\int_0^\pi \lambda_q(x,y,t)\sin(mx)\sin(ny)\mathrm{d}x\mathrm{d}y. \quad (36)$$

Given the initial value $\widetilde{W}_m(t_0)$ and $\dot{\widetilde{W}}_m(t_0)$ at the initial time $t_0 = 0$, Eq. (35) can be solved to obtain the center deflection–time relationship for the plate by employing the fourth-order Runge–Kutta method.

$$g_{40}\frac{\mathrm{d}^2(\varepsilon A_{11}^{(1)})}{\mathrm{d}t^2} + g_{41}\left(\varepsilon A_{11}^{(1)}\right) + g_{42}\left(\varepsilon A_{11}^{(1)}\right)^2 + g_{43}\left(\varepsilon A_{11}^{(1)}\right)^3 - \bar{\lambda}_q(x,y,t) = 0, \quad (35)$$

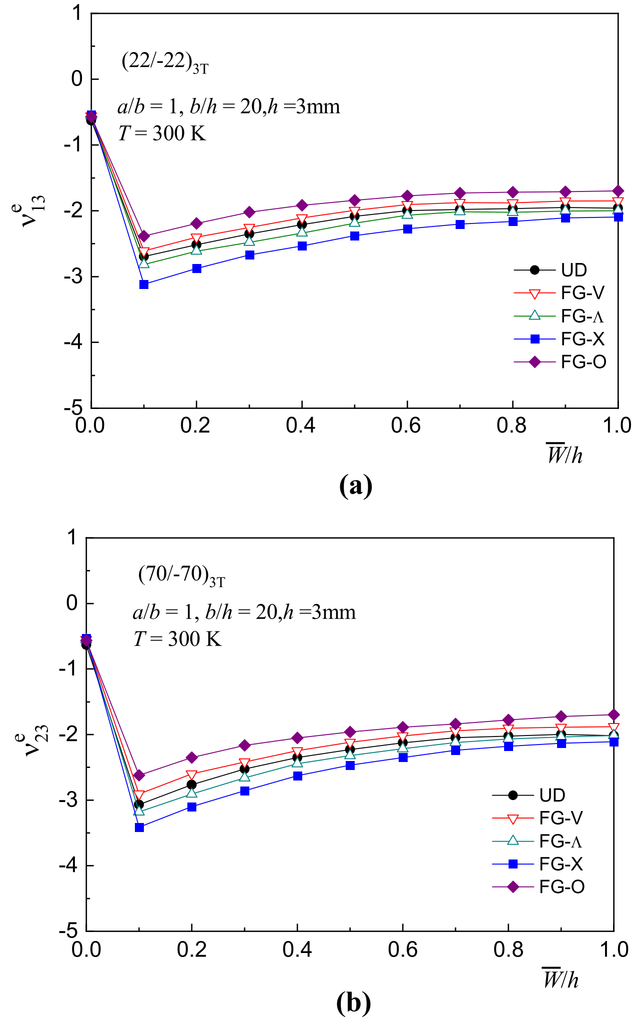


Fig. 13 EPR–deflections relationships of FG-CNTRC plates at reference temperature ($T=300$ K)

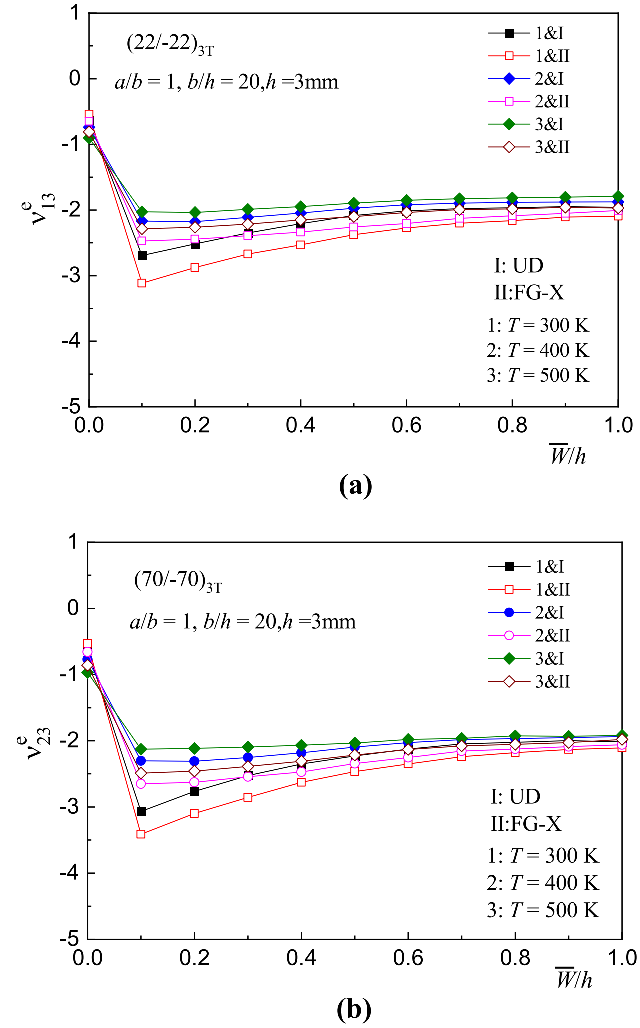


Fig. 14 EPR–deflections relationships of CNTRC plates at various temperatures

## 4 Numerical results and discussions

### 4.1 Verification studies

To verify the proposed model, two case studies are reported. Unless otherwise stated, immovable in-plane condition is considered in the following analysis. First, as a part of the verification of the proposed method and the finite element modeling, Fig. 7 shows the comparison of the solutions of a cross-ply square plate using the present method, finite element method and the method proposed by Reddy [47]. The dimensions and material properties of the square laminated plate are taken as: $a=25$ cm, $h=1$ cm, $E_1=52.5\times10^6$ N/cm, $E_2=2.1\times10^6$ N/cm, $G_{12}=G_{13}=1.05\times10^6$ N/cm, $G_{23}=4.2\times10^5$ MPa, $\nu_{12}=0.25$, $\rho=8\times10^{-6}$Ns$^2$/cm$^4$. In the forced vibration stage (time range 0–1 ms), the plate is subjected to a uniformly distributed load $q_0$. As described in Fig. 7, the dimensionless deflection ($\bar{w} = w_0\left(E_2h^3/q_0a^4\right) \times 10^2$) time curves agree well with the results of Reddy [47].

The second comparison is made for the forced vibrations of CNTRC plates with $a/h=10$, $b=a=25$ cm and $V_{CN}=0.11$. Constituent materials of the CNTRC plates are listed in Table 3. In Fig. 8, the results predicted by the present model are compared with the numerical results obtained from Lei et al. [34]. A theoretical model developed by Fan et al. [48] is also adopted as a benchmark. Good agreement can be observed between the existing results and the present method, which demonstrates the accuracy of the proposed model.

### 4.2 Parametric studies

After verifying the correctness of the present method, several case studies are conducted to estimate the effects of CNT distribution, temperature field, and foundation type on the dynamic response of FG-CNTRC plates. Let us examine the dynamic behavior with application to the above-discussed case of $(\pm 22)_{3T}$ and $(\pm 70)_{3T}$. Figure 9 exhibits the nonlinear dynamic response curves of UD and FG-CNTRC at the room temperature ($T = 300$ K). Five different distribution patterns mentioned above are taken into consideration. The value of the parameters used are: $a = 60$ mm, $h = 3$ mm. In addition, the curves of the UD pattern are used at the same temperature for reference. It can be observed that the FG-X plate has the lowest deflection among the five, while the uniformed distribution (UD) plate has the highest deflection. This is because increasing CNT volume fraction in the surface layer where the higher normal stresses occur can improve the bending stiffness of the plate. Note that UD and FG-X are also considered in the next parametric study.

The present approach is also used to investigate the influence of changing temperature field in UD and FG-X plates. Figure 10 describes the influence of the thermal stress on UD and FG-X plates. The applied load is 4 MPa for $(\pm 22)_{3T}$ and $(\pm 70)_{3T}$. Incremental temperatures are marked on these curves. The curves show that the amplitude and period of response increases with increase in temperature. This is attributed to the fact that increase in temperature leads to the weakening of the materials, thereby reducing the overall plate stiffness which in turn increases the central deflection.

Figure 11 reveals the maximum deflection with time variation of square antisymmetric laminates $(\pm 22)_{3T}$ and $(\pm 70)_{3T}$ for different elastic foundations stiffness ($(k_1, k_2) = (0, 0)$, $(10^2, 0)$, $(10^2, 10)$). Plates without the foundation ($k_1 = k_2 = 0$) are selected as a comparative example. It appears that the results confirm that the influence of foundation stiffness is to decrease the deflection. It means that the effective stiffness of FG-CNTRC plate enhances as the coefficients of foundation ($k_1$, $k_2$) enlarges, which would result in the decrement of the central deflection.

Figure 12 shows the deflection–time curves for movable edges conditions. The predicted results for three different initial edge loads are $P = P_{cr}\,(-0.5, 0, 0.5)$. $P_{\mathrm{cr}}$ refers to the critical load of the plates itself. In this case, $P = 0.5P_{\mathrm{cr}}$ and $P = -0.5P_{\mathrm{cr}}$, respectively, refer to the compressive and tensile loading. We can note that the compressive loading leads to an increase in the deflection; whereas, increasing tensile loading suppresses the maximum deflection.

The variations of EPR with dimensionless deflection ($\overline{W}/h$) for CNTRC laminated plates in the dynamic response region are obtained using numerical method and are shown in Figs. 13, 14. It can be found that the value of EPR first decreases and then increases smoothly with the increasing value of $\bar{W}/h$. Meanwhile, one can also see that the difference in the EPR is particularly small for the large values of $\overline{W}/h$. The FG-X plate has shown the lowest EPR–deflection curve and the curve from UD is positioned between FG-X and FG-O (see Fig. 13). Meanwhile, the variation of EPR tends to be flatter when the deflection has become sufficiently large. A similar trend can also be found in Fig. 14. Next, the EPRs of UD and FG-X plates under different temperatures are given. The EPR–deflection values of $(\pm 22)_{3T}$ and $(\pm 70)_{3T}$ increases when the temperature is increased between 300 and 500 K as shown in Fig. 14.

## 5 Conclusions

In this study, theoretical model for the nonlinear dynamic response of FG-CNTRC plates with various external conditions is proposed. The asymptotic solutions developed accounts for the functionally graded configurations and NPRs during the dynamic behavior of plates. Five types of volume fractions of the CNTs are considered which include UD, FG-$\Lambda$, FG-V, FG-X, and FG-O. The solutions for nonlinear dynamic responses are derived using a two-step perturbation approach by utilizing a fourth-order Runge–Kutta method. The influence of the temperature variation and elastic foundation stiffnesses on the dynamic behavior of CNTRC laminated plates is investigated in detail. The conclusions drawn may be summarized as:

- The $(\pm 22)_{3T}$ and $(\pm 70)_{3T}$ laminates attain a larger magnitude of NPR than those of the same thickness $(\pm\theta)_T$ or $(\pm\theta)_{2T}$ angle-ply laminates.
- Among the five types of CNTs distribution, the FG-X arrangement has the minimum central deflection, followed by FG-V&Λ, UD and FG-O, respectively. Moreover, the FG-X plate showed better performance than that with UD under different external conditions.

- A rise in temperature leads to increase in the central deflection; whereas, the increasing foundation stiffness will result in an opposite effect.
- For the plate subjected to initial edge loads, it is seen that initially tensile plates have the lowest central deflections; while the initially compressed plates have the highest central deflections.
- The EPR–deflection curves tend to be smooth when *W/h* is sufficiently large.

**Acknowledgements** The authors are also grateful for the supports from the Science Research Plan of Shanghai Municipal Science and Technology Committee under Grant 18DZ1205603, the National Key Research and Development Program of China [Grant No. 2017YFC0806100] and the National Natural Science Foundation of China [Grant No. 51908352].

## Compliance with ethical standards

**Conflict of interest** The authors declare that there are no conflicts of interests with publication of this work.

## Appendix 1

In Eqs. (9)–(12), the thermal resultants $\bar{N}_i^T$, $\bar{M}_i^T$ and $\bar{P}_i^T$ are given by

$$\begin{bmatrix} \bar{N}_x^T & \bar{M}_x^T & \bar{P}_x^T \\ \bar{N}_y^T & \bar{M}_y^T & \bar{P}_y^T \\ \bar{N}_{xy}^T & \bar{M}_{xy}^T & \bar{P}_{xy}^T \end{bmatrix} = \sum_{k=1}^{N} \int_{h_{k-1}}^{h_k} \begin{bmatrix} A_x \\ A_y \\ A_{xy} \end{bmatrix}_k (1, Z, Z^3)\Delta T \, \mathrm{d}Z, \tag{37a}$$

and $\bar{S}_i^T$, $(i = x, y, xy)$ are given as

$$\begin{bmatrix} \bar{S}_x^T \\ \bar{S}_y^T \\ \bar{S}_{xy}^T \end{bmatrix} = \begin{bmatrix} \bar{M}_x^T \\ \bar{M}_y^T \\ \bar{M}_{xy}^T \end{bmatrix} - \frac{4}{3h^2} \begin{bmatrix} \bar{P}_x^T \\ \bar{P}_y^T \\ \bar{P}_{xy}^T \end{bmatrix}, \tag{37b}$$

in which $\Delta T$ is temperature increment from an initial state ($T_0$), $\Delta T = T - T_0$, and

$$\begin{bmatrix} A_x \\ A_y \\ A_{xy} \end{bmatrix} = - \begin{bmatrix} \bar{Q}_{11} & \bar{Q}_{12} & \bar{Q}_{16} \\ \bar{Q}_{12} & \bar{Q}_{22} & \bar{Q}_{26} \\ \bar{Q}_{16} & \bar{Q}_{26} & \bar{Q}_{66} \end{bmatrix} \begin{bmatrix} c^2 & s^2 \\ s^2 & c^2 \\ 2cs & -2cs \end{bmatrix} \begin{bmatrix} \alpha_{11} \\ \alpha_{22} \end{bmatrix}, \tag{38}$$

where $\bar{Q}_{ij}$ are the component of the transformed lamina stiffness matrix which are evaluated as follows:

$$\begin{bmatrix} \bar{Q}_{11} \\ \bar{Q}_{12} \\ \bar{Q}_{22} \\ \bar{Q}_{16} \\ \bar{Q}_{26} \\ \bar{Q}_{66} \end{bmatrix} = \begin{bmatrix} c^4 & 2c^2s^2 & s^4 & 4c^2s^2 \\ c^2s^2 & c^4 + s^4 & c^2s^2 & -4c^2s^2 \\ s^4 & 2c^2s^2 & c^4 & 4c^2s^2 \\ c^3s & cs^3 - c^3s & -cs^3 & -2cs(c^2 - s^2) \\ cs^3 & c^3s - cs^3 & -c^3s & 2cs(c^2 - s^2) \\ c^2s^2 & -2c^2s^2 & c^2s^2 & (c^2 - s^2)^2 \end{bmatrix} \begin{bmatrix} Q_{11} \\ Q_{12} \\ Q_{22} \\ Q_{66} \end{bmatrix}, \tag{39a}$$

$$\begin{bmatrix} \bar{Q}_{44} \\ \bar{Q}_{45} \\ \bar{Q}_{55} \end{bmatrix} = \begin{bmatrix} c^2 & s^2 \\ -cs & cs \\ s^2 & c^2 \end{bmatrix} \begin{bmatrix} Q_{44} \\ Q_{55} \end{bmatrix}, \tag{39b}$$

where

$$\begin{aligned} &Q_{11} = E_{11}(1 - \nu_{12}\nu_{21})^{-1}, Q_{22} = E_{22}(1 - \nu_{12}\nu_{21})^{-1}, \\ &Q_{12} = \nu_{21}E_{11}(1 - \nu_{12}\nu_{21})^{-1} Q_{16} = Q_{26} = 0, \\ &Q_{66} = G_{12}, Q_{44} = G_{23}, Q_{55} = G_{13}. \end{aligned} \tag{40}$$

The coefficient $I_i$ can be calculated as:

$$(I_1, I_2, I_3, I_4, I_5, I_7) = \sum_{k=1}^{N} \int_{h_{k-1}}^{h_k} \rho_k \left(1, Z, Z^2, Z^3, Z^4, Z^6\right) \mathrm{d}Z, \tag{41a}$$

and

$$\begin{aligned} &\bar{I}_2 = I_2 - \frac{4I_4}{3h^2}, \bar{I}_5 = I_5 - \frac{4I_7}{3h^2}, \bar{I}_3 = I_3 - \frac{8I_5}{3h^2} + \frac{16I_7}{9h^4}, \\ &I_8 = \frac{I_2\bar{I}_2}{I_1} - \bar{I}_3 - \frac{4}{3h^2}\bar{I}_5, I_9 = \frac{4}{3h^2}\left(\bar{I}_5 - \frac{\bar{I}_2 I_4}{I_1}\right), I_{10} = \frac{\bar{I}_2\bar{I}_2}{I_1} - \bar{I}_3. \end{aligned} \tag{41b}$$

## Appendix 2

The matrices in the Eq. (17) are derived in Shen [49]

$$\begin{bmatrix} A_{ij}^* & B_{ij}^* & D_{ij}^* \\ E_{ij}^* & F_{ij}^* & H_{ij}^* \end{bmatrix} = \begin{bmatrix} A_{ij}^{-1} & -A_{ij}^{-1}B_{ij} & D_{ij} - B_{ij}A_{ij}^{-1}B_{ij} \\ -A_{ij}^{-1}E_{ij} & F_{ij} - E_{ij}A_{ij}^{-1}B_{ij} & H_{ij} - E_{ij}A_{ij}^{-1}E_{ij} \end{bmatrix}, (i,j = 1, 2, 6), \tag{42}$$

in which $A_{ij}$, $B_{ij}$, $D_{ij}$, etc. refer to the plate stiffnesses, which are functions of $(\bar{Q}_{ij})_k$

$$\left(A_{ij},B_{ij},D_{ij},E_{ij},F_{ij},H_{ij}\right)=\sum_{k=1}^{N}\int_{h_{k-1}}^{h_k}(\bar{Q}_{ij})_k\left(1,Z,Z^2,Z^3,Z^4,Z^6\right)\mathrm{d}Z\ (i,j=1,2,6),\tag{43a}$$

$$\left(A_{ij},D_{ij},F_{ij}\right)=\sum_{k=1}^{N}\int_{h_{k-1}}^{h_k}(\bar{Q}_{ij})_k(1,Z^2,Z^4)\mathrm{d}Z\ (i,j=4,5)(i,j=4,5),\tag{43b}$$

In the general case, the matrices $A^*_{ij}$,$D^*_{ij}$ and $H^*_{ij}$ are symmetric although the matrices $B^*_{ij}$,$E^*_{ij}$ and $F^*_{ij}$ might be not.

In the case of $(\pm\theta)_{3T}$ laminated plate:

$$\begin{cases} A_{45}=D_{45}=F_{45}=0\\ F^*_{61}=F^*_{62}=B^*_{66}=E^*_{66}=0\end{cases}\quad \begin{cases} A^*_{ij}=D^*_{ij}=F^*_{ij}=H^*_{ij}=0(i=1,2;j=6)\\ B^*_{ij}=E^*_{ij}=0\qquad (i,j=1,2)\end{cases}\tag{44}$$

## Appendix 3

In Eq. (35),

$$g_{40}=-\left[\gamma_{170}-\gamma_{171}(m^2+n^2\beta^2)\right]-g^*_{08}-\gamma_{14}\gamma_{24}m^2n^2\beta^2\frac{g^*_{05}g_{07}}{g_{06}}+\gamma_{80}\left(\gamma_{14}\gamma_{24}\frac{m^2g_{02}+n^2\beta^2g_{01}}{g_{00}}\frac{g_{05}}{g_{06}}-\frac{m^2g_{04}+n^2\beta^2g_{03}}{g_{00}}\right),\tag{45}$$

$$g_{41}=\begin{cases} Q_{11}-\gamma_{14}(\gamma_{T1}m^2+\gamma_{T2}n^2\beta^2)\Delta T+3g_{43}\Phi^2(T)\ (immovable)\\ Q_{11}\left[1-\frac{P}{P_{cr}}\frac{(m^2+\eta n^2\beta^2)}{m^2}\right]\qquad (\text{movable}),\end{cases}\tag{46}$$

$$g_{42}=3g_{43}\Phi(T),g_{43}=\frac{\gamma_{14}\gamma_{24}}{16}\left(\frac{m^4}{\gamma_7}+\frac{n^4\beta^4}{\gamma_6}+C_{33}\right),\tag{47}$$

$$C_{33}=\begin{cases} 2\frac{m^4+\gamma_{24}^2n^4\beta^4+2\gamma_5m^2n^2\beta^2}{\gamma_{24}^2-\gamma_5^2}\ (\text{immovable})\\ 0\qquad (\text{movable})\end{cases},\tag{48}$$

where the other symbols are given in Shen [45]

$$Q_{11}=g_{08}+\gamma_{14}\gamma_{24}m^2n^2\beta^2\frac{g_{05}g_{07}}{g_{06}}+\left[K_1+K_2(m^2+n^2\beta^2)\right],\quad \gamma_6=1+\frac{4m^2\gamma_{14}\gamma_{24}\gamma^2_{230}}{\gamma_{42}+\gamma_{430}4m^2},\gamma_7=\gamma^2_{24}+\frac{4n^2\beta^2\gamma_{14}\gamma_{24}\gamma^2_{223}}{\gamma_{31}+\gamma_{322}4n^2\beta^2},\tag{49}$$

$$\Phi(T)=\lambda+\Theta_3(\lambda)^3+\cdots\tag{50}$$

The coefficients $\lambda$ and $\Theta_3$ can be obtained as follow for $m=n=1$

$$\begin{aligned}\lambda&=\frac{16}{\pi^2G_{08}}\left((\gamma_{T3}m^2+\gamma_{T4}n^2\beta^2)-\frac{(\gamma_{T3}-\gamma_{T6})m^2g_{102}+(\gamma_{T4}-\gamma_{T7})n^2\beta^2g_{101}}{g_{00}}\right)\Delta T\times\frac{h}{\left[D^*_{11}D^*_{22}A^*_{11}A^*_{22}\right]^{1/4}},\\ \Theta_3&=-\frac{\gamma_{14}\gamma_{24}}{16G_{08}}\left(\frac{m^4}{\gamma_7}+\frac{n^4\beta^4}{\gamma_6}+C_{33}\right),\\ \begin{bmatrix}g_{101}\\ g_{102}\end{bmatrix}&=\begin{bmatrix}\left(\gamma_{31}+\gamma_{320}m^2+\gamma_{322}n^2\beta^2\right)\left(\gamma_{230}m^2+\gamma_{232}n^2\beta^2\right)-\gamma_{331}n^2\beta^2\left(\gamma_{221}m^2+\gamma_{223}n^2\beta^2\right)\\ \left(\gamma_{42}+\gamma_{430}m^2+\gamma_{432}n^2\beta^2\right)\left(\gamma_{221}m^2+\gamma_{223}n^2\beta^2\right)-\gamma_{331}m^2\left(\gamma_{230}m^2+\gamma_{232}n^2\beta^2\right)\end{bmatrix},\\ G_{08}&=Q_{11}-\gamma_{14}\left(\gamma_{T1}m^2+\gamma_{T2}n^2\beta^2\right)\Delta T.\end{aligned}\tag{51}$$

## References


1. Sun C-T, Whitney JM (1973) Theories for the dynamic response of laminated plates. Aiaa J 11:178–183
2. Ramkumar RL, Chen PC (1983) Low-velocity impact response of laminated plates. Aiaa J 21:1448–1452
3. Reddy JN (1983) Geometrically nonlinear transient analysis of laminated composite plates. Aiaa J 21:621–629
4. Huang X-L, Shen H-S (2004) Nonlinear vibration and dynamic response of functionally graded plates in thermal environments. Int J Solids Struct 41:2403–2427
5. Mallek H, Jrad H, Wali M, Dammak F (2019) Nonlinear dynamic analysis of piezoelectric-bonded FG-CNTR composite structures using an improved FSDT theory. Eng Comput. https://doi.org/10.1007/s00366-019-00891-1
6. Li C, Shen H-S, Wang H (2019) Nonlinear dynamic response of sandwich beams with functionally graded negative Poisson's ratio honeycomb core. Eur Phys J Plus 134:79–94
7. Nguyen DD, Pham CH (2016) Nonlinear dynamic response and vibration of sandwich composite plates with negative Poisson's ratio in auxetic honeycombs. J Sandw Struct Mater 20:692–717
8. Zhang RG, Yeh H-L, Yeh H-Y (1998) A preliminary study of negative Poisson's ratio of laminated fiber reinforced composites. J Reinf Plast Compos 17:1651–1664
9. Evans KE, Donoghue JP, Alderson KL (2004) The design, matching and manufacture of auxetic carbon fibre laminates. J Compos Mater 38:95–106
10. Lempriere MB (1968) Poisson's ratio in orthotropic materials. Aiaa J 6:2226–2227

11. Clarke JF, Duckett RA, Hine PJ, Hutchinson IJ, Ward IM (1994) Negative Poisson's ratios in angle-ply laminates: theory and experiment. Composites 25:863–868
12. Herakovich CT (1984) Composite laminates with negative through-the-thickness. J Compos Mater 18:447–455
13. Hine PJ, Duckett RA, Ward IM (1997) Negative Poisson' s ratios in angle-ply laminates. J Mater Sci Lett 16:541–544
14. Matsuda T, Goto K, Kubota N, Ohno N (2014) Negative through-the-thickness Poisson's ratio of elastic–viscoplastic angle-ply carbon fiber-reinforced plastic laminates: homogenization analysis. Int J Plast 63:152–169
15. Hadi Harkati E, Bezazi A, Scarpa F, Alderson K, Alderson A (2007) Modelling the influence of the orientation and fibre reinforcement on the Negative Poisson's ratio in composite laminates. Phys Stat Sol (b) 244:883–892
16. Hadi Harkati E, Bezazi A, Boukharouba W, Scarpa F (2009) Influence of carbon fibre on the through-the-thickness NPR behaviour of composite laminates. Phys stat sol (b) 246:2111–2117
17. Sun C-T, Li SJ (1988) Three-dimensional effective elastic constants for thick laminates. J Compos Mater 22:629–639
18. Kolahchi R, Safari M, Esmailpour M (2016) Dynamic stability analysis of temperature-dependent functionally graded CNT-reinforced visco-plates resting on orthotropic elastomeric medium. Compos Struct 150:255–265
19. Hajmohammad MH, Kolahchi R, Zarei MS, Maleki M (2018) Earthquake induced dynamic deflection of submerged viscoelastic cylindrical shell reinforced by agglomerated CNTs considering thermal and moisture effects. Compos Struct 187:498–508
20. Lyu Z, Yang Y, Liu H (2020) High-accuracy hull iteration method for uncertainty propagation in fluid-conveying carbon nanotube system under multi-physical fields. Appl Math Model 79:362–380
21. Reddy JN, Khdeir AA (1989) Dynamic response of cross-ply laminated shallow shells according to a refined shear deformation theory. J Acoust Soc Am 85:2423–2431
22. Khalili SMR, Jafari AA, Eftekhari SA (2010) A mixed Ritz-DQ method for forced vibration of functionally graded beams carrying moving loads. Compos Struct 92:2497–2511
23. Fan Y, Xiang Y, Shen H-S (2020) Nonlinear dynamics of temperature-dependent FG-GRC laminated beams resting on visco-pasternak foundations. Int J Struct Stab Dy 20:2050012
24. Gong SW, Lam KY, Reddy JN (1999) The elastic response of functionally graded cylindrical shells to low-velocity impact. Int J Impact Eng 22:397–417
25. Kiani Y, Sadighi M, Salami SJ, Eslami MR (2013) Low velocity impact response of thick FGM beams with general boundary conditions in thermal field. Compos Struct 104:293–303
26. Fan Y, Xiang Y, Shen H-S, Hui D (2018) Nonlinear low-velocity impact response of FG-GRC laminated plates resting on visco-elastic foundations. Compos B Eng 144:184–194
27. Liu H, Lv Z, Wu H (2019) Nonlinear free vibration of geometrically imperfect functionally graded sandwich nanobeams based on nonlocal strain gradient theory. Compos Struct 214:47–61
28. Wu H, Liu H (2020) Nonlinear thermo-mechanical response of temperature-dependent FG sandwich nanobeams with geometric imperfection. Eng Comput. https://doi.org/10.1007/s00366-020-01005-y
29. Liu H, Wu H, Lyu Z (2020) Nonlinear resonance of FG multilayer beam-type nanocomposites: effects of graphene nanoplatelet-reinforcement and geometric imperfection. Aerosp Sci Technol 98:105702
30. Shen H-S (2009) Functionally graded materials nonlinear analysis of plates and shells. CRC Press, Boca Raton
31. Shen H-S (2009) Nonlinear bending of functionally graded carbon nanotube-reinforced composite plates in thermal environments. Compos Struct 91:9–19
32. Wang Z-X, Shen H-S (2012) Nonlinear dynamic response of nanotube-reinforced composite plates resting on elastic foundations in thermal environments. Nonlinear Dyn 70:735–754
33. Fan Y, Wang H (2017) Nonlinear low-velocity impact on damped and matrix-cracked hybrid laminated beams containing carbon nanotube reinforced composite layers. Nonlinear Dyn 89:1863–1876
34. Lei ZX, Zhang LW, Liew KM (2015) Elastodynamic analysis of carbon nanotube-reinforced functionally graded plates. Int J Mech Sci 99:208–217
35. Zhang LW, Xiao LN, Zou GL, Liew KM (2016) Elastodynamic analysis of quadrilateral CNT-reinforced functionally graded composite plates using FSDT element-free method. Compos Struct 148:144–154
36. Thanh NV, Khoa ND, Tuan ND, Tran P, Duc ND (2017) Nonlinear dynamic response and vibration of functionally graded carbon nanotube-reinforced composite (FG-CNTRC) shear deformable plates with temperature-dependent material properties and surrounded on elastic foundations. J Therm Stress 40:1254–1274
37. Phung-Van P, Thanh C, Nguyen-Xuan H, Abdel-Wahab M (2018) Nonlinear transient isogeometric analysis of FG-CNTRC nanoplates in thermal environments. Compos Struct 201:882–892
38. Ebrahimi F, Farazmandnia N, Kokaba MR, Mahesh V (2019) Vibration analysis of porous magneto-electro-elastically actuated carbon nanotube-reinforced composite sandwich plate based on a refined plate theory. Eng Comput. https://doi.org/10.1007/s00366-019-00864-4
39. Yeh H-L, Yeh H-Y (2002) The effect of transverse moduli on dilatation and through-thickness Poisson' s ratio in angle-ply laminates. J Reinf Plast Compos 21:1653–1670
40. Zhang LW, Memar Ardestani M, Liew KM (2017) Isogeometric approach for buckling analysis of CNT-reinforced composite skew plates under optimal CNT-orientation. Compos Struct 163:365–384
41. Jam JE, Sh M (2011) Elastic buckling of composite plate reinforced with carbon nanotubes. Inter J Eng Sci Technol 3:4090–4101
42. Zhang RG, Yeh H-L, Yeh H-Y (1998) A preliminary study of negative Poisson's ratio of laminated fiber reinforced composites. 17:1651–1664
43. Yeh H-L, Yeh H-Y (1999) A discussion of negative Poisson's ratio design for composites. J Reinf Plast Compos 18:1546–1556
44. Reddy JN (1984) A simple higher-order theory for laminated composite plates. J Appl Mech 51:745–752
45. Shen H-S (2013) A two-step perturbation method in nonlinear analysis of beams, plates and shells. Wiley, Singapore
46. Shen H-S, Huang X-H, Yang J (2020) Nonlinear bending of temperature-dependent FG- CNTRC laminated plates with negative Poisson' s ratio. Mech Adv Mater Struc 27:1–13
47. Reddy JN (1997) Mechanics of laminated composite plates: theory and analysis. CRC Press, Boca Raton, FL
48. Fan Y, Xiang Y, Shen H-S (2019) Nonlinear forced vibration of FG-GRC laminated plates resting on visco-Pasternak foundations. Compos Struct 209:443–452
49. Shen H-S (1997) Kármán-type equations for a higher-order shear deformation plate theory and its use in the thermal postbuckling analysis. Appl Math Mech 18:1137–1152